

Article

In Situ ZrB₂ Formation in B₄C Ceramics and Its Strengthening Mechanism on Mechanical Properties

Wankai Yao ¹, Junbing Yan ², Xiangcheng Li ^{1,*} , Pingan Chen ^{1,*}, Yingli Zhu ¹ and Boquan Zhu ¹

¹ The State Key Laboratory of Refractories and Metallurgy, Wuhan University of Science and Technology, Wuhan 430081, China

² Wuhan Xinxin Semiconductor Manufacturing Co., Ltd., Wuhan 430223, China

* Correspondence: lixiangcheng@wust.edu.cn (X.L.); pinganchen@wust.edu.cn (P.C.)

Abstract: In order to reduce the sintering temperature and improve the mechanical properties of B₄C ceramics, ZrB₂ was formed in situ using the SPS sintering method with ZrO₂ and B₄C as raw materials. Thermodynamic calculations revealed that CO pressure affected the formation of ZrB₂ at temperatures from 814 °C to 1100 °C. The experimental results showed that the ZrB₂ grain size was <5 μm and that the grains were uniformly distributed within the B₄C ceramics. With an increase in ZrO₂ content, the Vickers hardness and flexural strength of the B₄C ceramics first increased and then decreased, while the fracture toughness continuously increased. When the content of ZrO₂ was 15 wt%, the Vickers hardness, fracture toughness and flexural strength of B₄C ceramics were 35.5 ± 0.63 GPa, 3.6 ± 0.24 MPa·m^{1/2} and 403 ± 10 MPa, respectively. These results suggest that ZrB₂ inhibits B₄C grain growth, eliminates crack tip stress, and provides fine grain to strengthen and toughen B₄C ceramics.

Keywords: spark plasma sintering (SPS); boron carbide (B₄C); Zirconium Diboride (ZrB₂); reaction sintering



Citation: Yao, W.; Yan, J.; Li, X.; Chen, P.; Zhu, Y.; Zhu, B. In Situ ZrB₂ Formation in B₄C Ceramics and Its Strengthening Mechanism on Mechanical Properties. *Materials* **2022**, *15*, 7961. <https://doi.org/10.3390/ma15227961>

Academic Editor: Alberto Ortona

Received: 8 October 2022

Accepted: 8 November 2022

Published: 10 November 2022

Publisher's Note: MDPI stays neutral with regard to jurisdictional claims in published maps and institutional affiliations.



Copyright: © 2022 by the authors. Licensee MDPI, Basel, Switzerland. This article is an open access article distributed under the terms and conditions of the Creative Commons Attribution (CC BY) license (<https://creativecommons.org/licenses/by/4.0/>).

1. Introduction

Due to their low density, high hardness and high elastic modulus, boron carbide (B₄C) ceramics have been used in the manufacturing of armor, cutting tools and neutron absorbers [1–5]. However, further application of B₄C ceramics is limited by the high sintering temperature (>2000 °C) and low fracture toughness ($K_{IC} < 2.2 \text{ MPa}\cdot\text{m}^{1/2}$), which can be attributed to the strong B-C covalent bonds, low atomic diffusion coefficient and low dislocation plasticity [6–10]. Therefore, it is essential to lower the sintering temperature and improve the mechanical properties of B₄C ceramics.

The addition of second phases, such as SiC, Al₂O₃, TiC and TiO₂, is an effective method of reducing the sintering temperature and improving the mechanical properties of B₄C ceramics [11,12], but ultimately results in reduced material hardness. Moreover, brittle compounds are formed during the densification process, leading to a low fracture toughness. Transitional metal diborides (TiB₂, ZrB₂) are useful additives which have similar properties to B₄C ceramics [13–15]. Among them, Zirconium Diboride (ZrB₂) has a high melting point (3245 °C), high hardness (14–23 GPa) and high flexural strength (higher than 500 MPa), which could improve the flexural strength and fracture toughness of B₄C ceramics [16,17].

Many reports have shown that the addition of ZrB₂ could efficiently enhance the mechanical properties of B₄C ceramics. For example, He et al. [18] found that ZrB₂ promoted the sintering process and increased the ceramic's high critical crack size, resulting in excellent thermal shock resistance. In order to inhibit the grain growth of B₄C, Lin et al. [19] prepared B₄C ceramics by pressureless sintering using ZrO₂ as a sintering aid. The in situ formation of ZrB₂ inhibited the abnormal growth of B₄C grains, prolonged the

crack extension path and improved the sintering activity. Guo et al. [20] prepared B₄C-ZrB₂ ceramics at low temperature, resulting in an average B₄C grain size of 1–2 μm. The hardness and fracture toughness reached 33.0 ± 1.3 GPa and 4.1 ± 0.2 MPa·m^{1/2}, respectively. Rehman et al. [21] prepared B₄C ceramics by SPS at 1700 °C; the average grain size of ZrB₂ was 1.3 ± 0.2 μm. The Vickers hardness, fracture toughness and flexural strength were 31.28 GPa, 4.2 MPa·m^{1/2} and 511 MPa, respectively. However, the role of ZrB₂ as a sintering aid and grain growth inhibitor requires further investigation, and the effect of ZrB₂ on the fracture mode transformation of B₄C ceramics also needs to be clarified.

In this work, we aim to obtain densified B₄C ceramics with the in situ formation of ZrB₂ at 1700 °C using the spark plasma sintering (SPS) method, with ZrB₂ grains homogeneously distributed in the B₄C ceramics. The reaction between ZrO₂ and B₄C could effectively reduce the sintering temperature, and the pinning effect of ZrB₂ is expected to inhibit the B₄C grain growth, achieving desirable mechanical properties.

2. Materials and Methods

2.1. Materials and Processes

B₄C powder (1 μm, analytically pure) and nano-ZrO₂ (50 nm, purity > 99.9%) were used as raw materials. Nano-Y₂O₃ (50 nm, purity > 99.9%) was used as a sintering aid.

The compositions of the samples are shown in Table 1. The raw materials were mixed with stainless steel balls in anhydrous ethanol with a ball-to-material ratio of 5:1 and a mixing time of 6 h at 250 r/min. After mixing, the mixtures were dried in a drying oven at 80 °C for 24 h and then passed through a 200-mesh sieve. Then, the mixtures were sintered by SPS (Dr. Sinter-3.20 MKII, Sumitomo, Tokyo, JPN) under vacuum. The heating rate was maintained at 100 °C/min and a uniaxial load of 5 kN was applied during the heating stage to ensure good contact conductivity with the graphite indenter. After the temperature rose to 1600 °C, the uniaxial load was slowly increased to 15 kN. Then, the sintering temperature was increased to 1700 °C for 6 min. The sintered ceramics were cooled in the furnace to about 150 °C and the samples were taken out to obtain B₄C ceramics.

Table 1. Compositions of samples.

Samples	BZ0	BZ5	BZ10	BZ15	BZ20
B ₄ C/wt%	100	95	90	85	80
ZrO ₂ /wt%	0	5	10	15	20
Y ₂ O ₃ /wt%	3	3	3	3	3

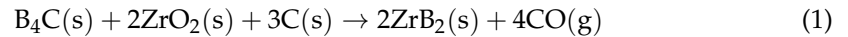
2.2. Characterizations

The bulk density of B₄C ceramics was measured using the Archimedes method. The Vickers hardness and fracture toughness were measured by the indentation method using a Vickers hardness tester (HV-50A, Huayin, Laizhou, China). The spacing between each indentation was ensured to be greater than 100 μm to avoid crack deformation or the overlapping of extended areas caused by indentation. Five effective indentations were also used to calculate the mean and error of Vickers hardness and fracture toughness. The B₄C ceramics were processed into long strip samples of 2 mm × 3 mm × 20 mm using a diamond wire cutting machine, and the bending strength of the samples was measured using a three-point bending test with a span of 16 mm and a loading rate of 0.5 mm/min. The mean values of flexural strength and error analyses were calculated with 3 sets of valid data. The phase compositions were characterized by X-ray diffractometer (XRD, X'Pert MPD Pro, Philips, Amsterdam, The Netherlands). The voltage and current of the Cu Kα1 radiation were 40 kV and 40 mA, respectively. The scanning range (2θ) was 10°–90°. The microscopic morphologies were characterized using a field-emission scanning electron microscope (FESEM, Nova NanoSem 400, Thermo, Waltham, MA, USA).

3. Results and Discussion

3.1. Thermodynamic Calculations

The in situ generation of ZrB₂ from B₄C and nano-ZrO₂ is represented in Reaction (1):



According to thermodynamic calculations by FactSage, the variation in Gibbs' free energy of reaction (1) as a function of temperature at different P_{CO} (pressure of CO) and as a function of P_{CO} at different temperatures is shown in Figure 1. Figure 1a shows that in the standard state ($P_{\text{CO}} = 0.986$ atm), a temperature above 1212 °C is favorable for the formation of ZrB₂. It is expected that reaction (1) proceeds more rapidly when the reaction is carried out under vacuum. Therefore, pure ZrB₂ can be synthesized at a temperature as low as 814 °C when $P_{\text{CO}} = 10^{-5}$ atm, according to Figure 1a. However, the CO generated by the sample surrounded by graphite die cannot be expelled in time, leading to $P_{\text{CO}} > 10^{-4}$ atm; thus, the reaction will proceed at a temperature higher than 814 °C. Figure 1b further illustrates that reaction (1) needs to proceed at temperatures above 1100 °C when P_{CO} is in the range of 0–0.1 atm. In the experiments, the vacuum pump worked continuously and the vacuum level in the furnace was as low as 8×10^{-5} atm during SPS, maintaining the P_{CO} at a low level and thus promoting the low-temperature densification of B₄C ceramics.

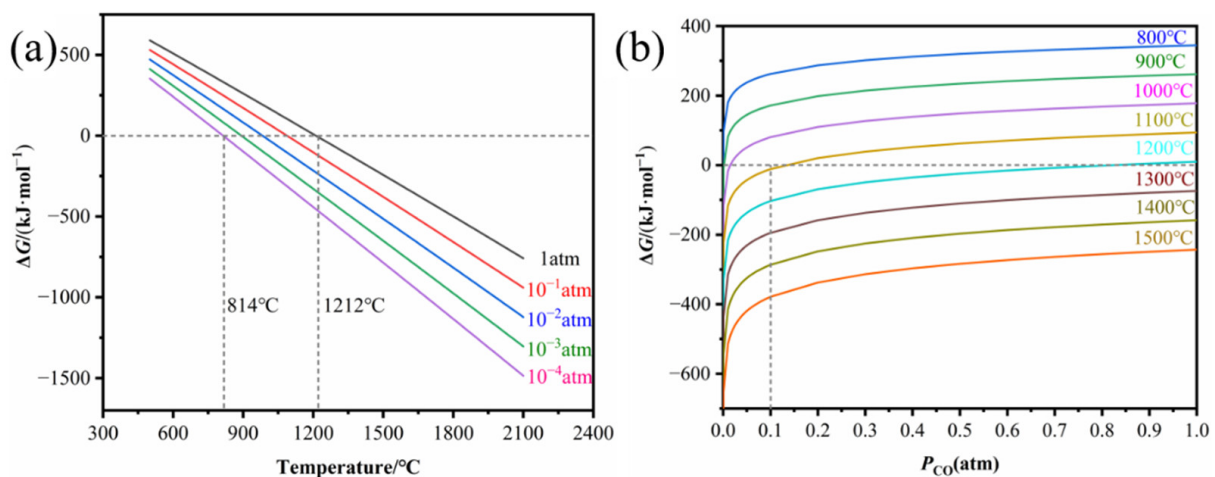


Figure 1. Gibbs' free energy change of reaction (1). (a) Variation in temperature at different P_{CO} ; (b) variation with P_{CO} at different temperatures.

3.2. XRD Phase Analysis

The XRD patterns of B₄C ceramics prepared by SPS with different ZrB₂ contents are shown in Figure 2. The ceramics are composed of B₄C and ZrB₂, and no residual nano-ZrO₂ phase can be detected, indicating that nano-ZrO₂ and B₄C completely reacted to form the ZrB₂ phase. The B₄C in the samples all had the rhombohedral crystal structure (PDF #35-0798). The diffraction peaks of samples at 2θ of 21.21°, 32.64°, and 41.69° were all taken from the ZrB₂ crystal (PDF #89-3930), and correspond to the (110), (200) and (211) crystal planes of its hexagonal crystal structure, respectively. The intensity of the ZrB₂ diffraction peak increases with the addition of nano-ZrO₂, while the intensity of the B₄C diffraction peak is the opposite, which is consistent with the expected results. The XRD results indicate that nano-ZrO₂ can react with B₄C in situ to form ZrB₂, which can promote the diffusion effect between B₄C particles during sintering and achieve the densification of B₄C ceramics.

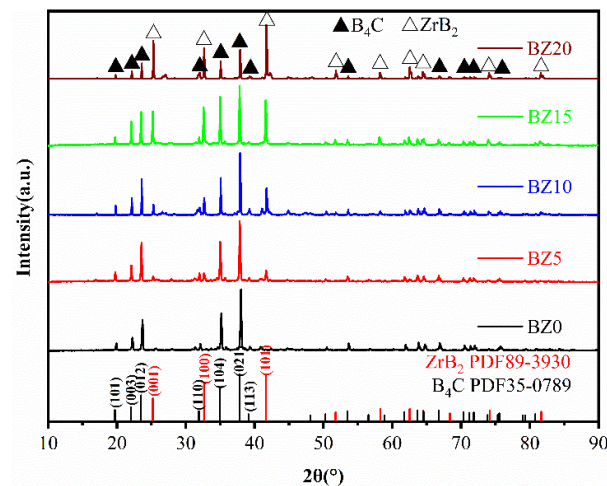


Figure 2. XRD patterns of B_4C ceramics with different nano- ZrO_2 contents.

3.3. Microstructural Analysis

The BSE images of B_4C ceramics and the grain size of ZrB_2 prepared by SPS are shown in Figure 3. The distribution of B, C and Ti elements in sample BZ15 are shown in Figure 3f–i. Combined with XRD, it can be deduced that the dark gray phase is B_4C , and the bright white phase is ZrB_2 . Figure 3a shows that the addition of 3 wt% nano- Y_2O_3 can achieve a polished surface of B_4C ceramics with no obvious pores without the addition of nano- ZrO_2 . Figure 3b–e show that the amount of ZrB_2 produced gradually increases as the addition of nano- ZrO_2 increases from 5 wt% to 20 wt%, and the average particle size of ZrB_2 increases from 1.03 μm to 1.37 μm . The in situ reaction of nano- ZrO_2 to generate ZrB_2 facilitates the flowability between B_4C particles and promotes the densification and pore discharge of B_4C ceramics, such that there are no obvious pores on the polished surface. In addition, ZrB_2 not only has small grain size, but is also uniformly distributed within the B_4C ceramics, which will effectively improve the mechanical properties.

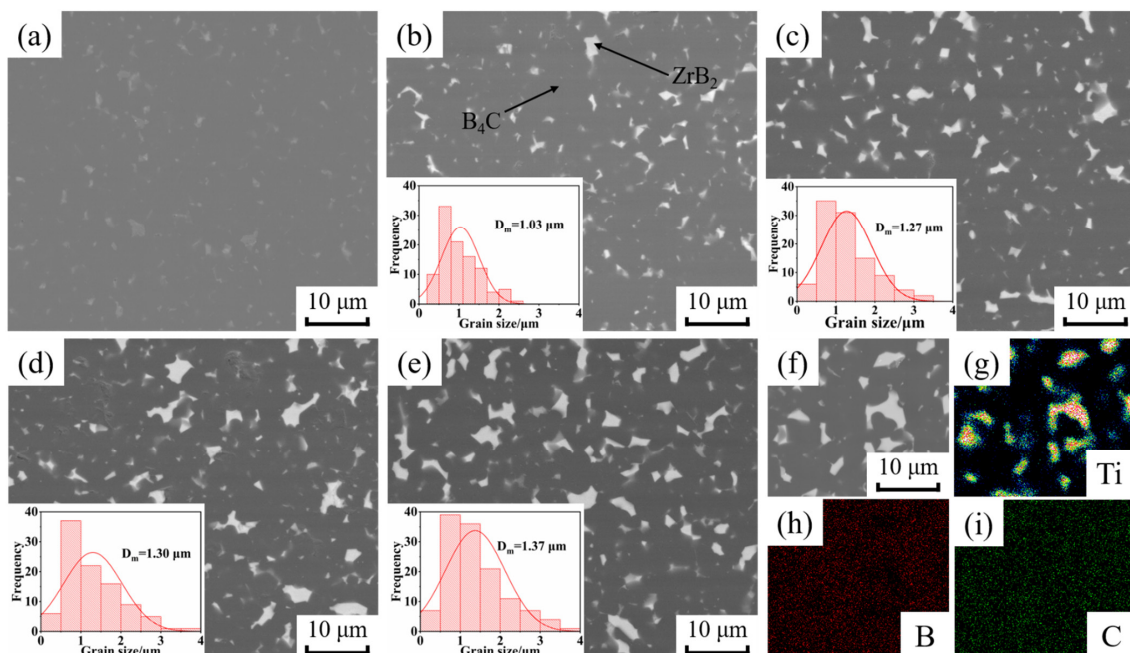


Figure 3. BSE images of B_4C ceramics and grain size of ZrB_2 . (a) BZ0, (b) BZ5, (c) BZ10, (d) BZ15, (e) BZ20 (f) BSE image of BZ15; element of Ti (g), B (h) and C (i).

BSE diagrams of the fracture morphology of B_4C ceramics with different nano- ZrO_2 contents are shown in Figure 4. The fracture mode is mainly through crystal fracture, and the fracture surface is relatively neat and smooth. This indicates a favorable degree of connection between the grains after SPS. In addition, there are more pores in the BZ0 sample, but the number of pores decreases significantly with the addition of nano- ZrO_2 . This indicates that nano- ZrO_2 promotes the densification of B_4C ceramics.

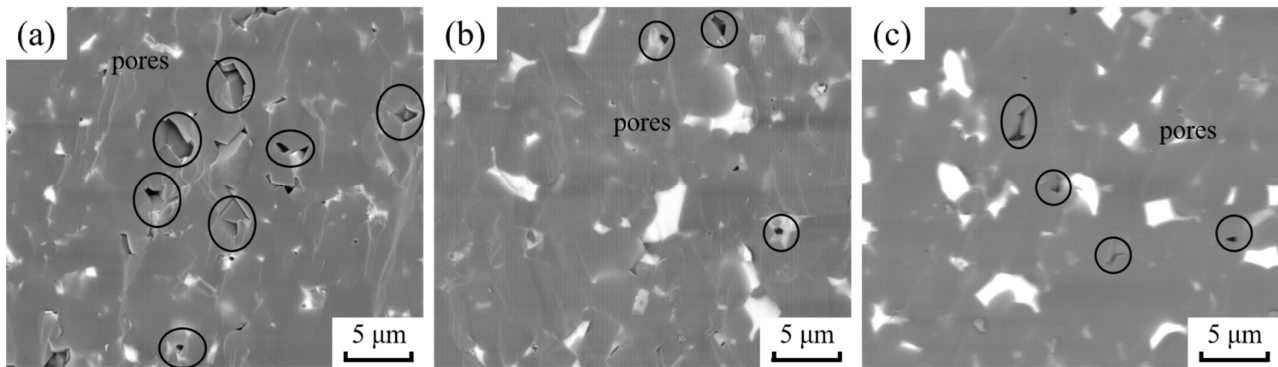


Figure 4. BSE diagrams of B_4C ceramics' fracture morphology. (a) BZ0; (b) BZ10; (c) BZ20.

TEM images of BZ15 are shown in Figure 5. Figure 5a shows the interface between B_4C and ZrB_2 in the B_4C ceramics. The HRTEM image shown in Figure 5b indicates that the grain boundary between B_4C ($d = 0.3781$ nm, (012) zone axis) and ZrB_2 ($d = 0.2166$ nm, (101) zone axis) is clean. This result indicates that the grain boundary strength between B_4C and ZrB_2 is strong. It is well-known that a high binding force between the matrix phase and second phase has a significant effect on mechanical properties. Therefore, this suggests that excellent mechanical properties can be obtained from these B_4C ceramic samples.

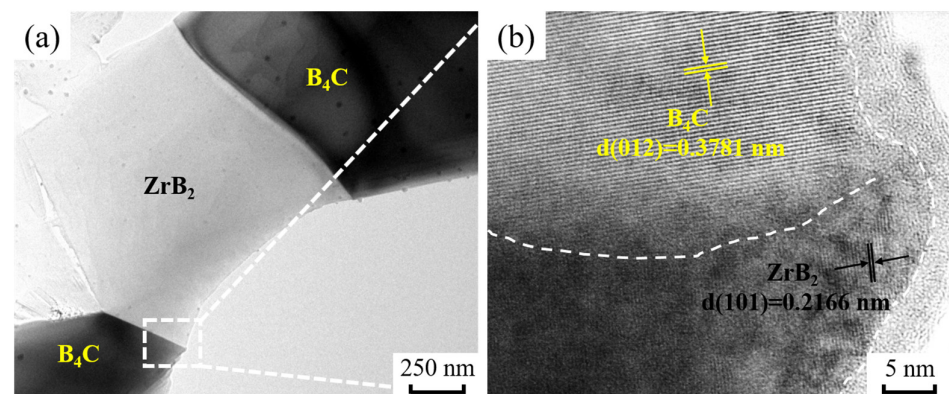


Figure 5. TEM diagrams of BZ15. (a) TEM; (b) HRTEM.

3.4. Mechanical Properties of the B_4C Ceramics

The relative density and bulk density of B_4C ceramics prepared by SPS with different ZrO_2 contents are shown in Figure 6. The relative densities measured are all above 98.3%, and increase and then decrease with increasing ZrO_2 content. The bulk density continues to increase, between 2.52 g/cm³ and 2.83 g/cm³. The relative density reaches a maximum of 99.6% when the content of ZrO_2 is 5 wt%; this can be attributed to the in situ reaction of nano- ZrO_2 to generate ZrB_2 , which that promotes the flowability between B_4C particles and obtains dense ceramics. When the content of ZrO_2 is higher than 5 wt%, the CO gas generated by the sintering reaction also increases, causing the relative density to decrease. The observed increase in bulk density can be explained by the fact that the theoretical density of ZrB_2 (6.1 g/cm³) is greater than that of B_4C , meaning that an increase in ZrB_2 content leads to a gradual increase in the bulk density of the ceramics.

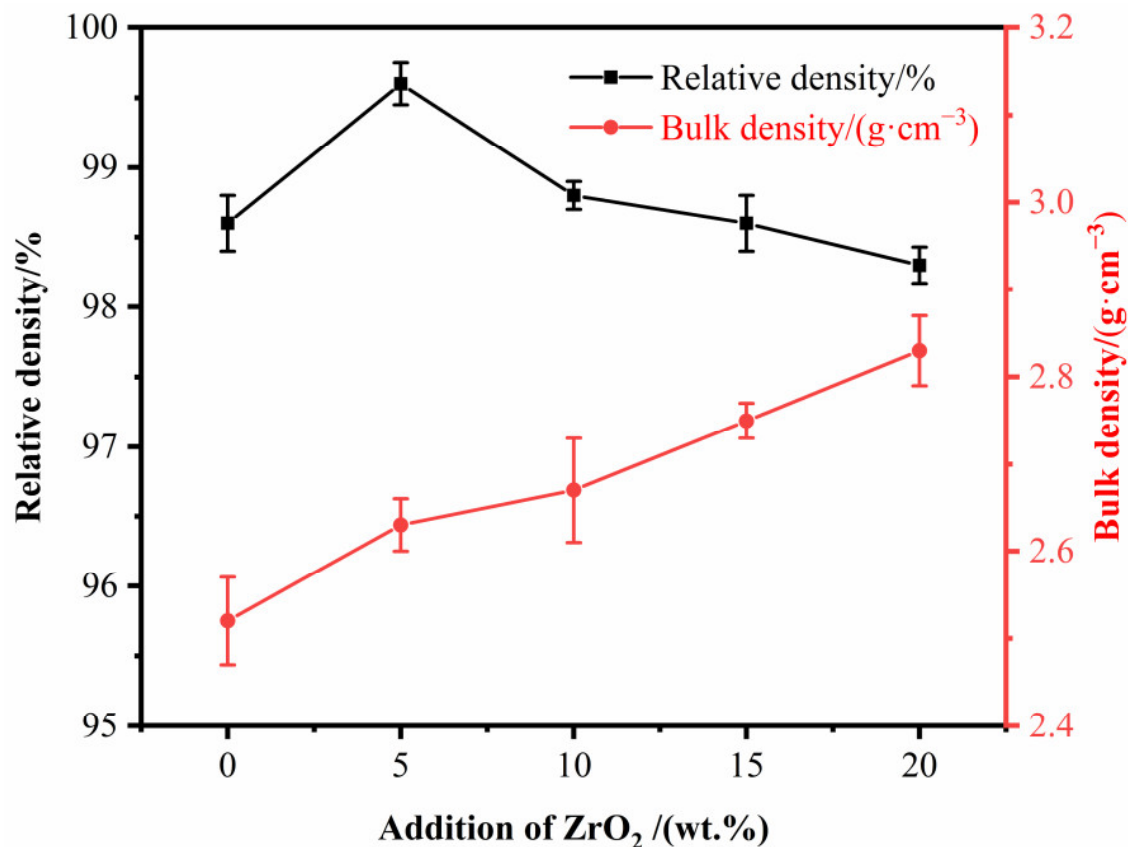


Figure 6. Relative density and bulk density of B₄C ceramics at different ZrB₂ contents.

The Vickers hardness, fracture toughness and flexural strength of B₄C ceramics prepared by SPS at different ZrO₂ contents are shown in Figure 7. From Figure 7a, it can be seen that with the increase of ZrO₂ content, the Vickers hardness shows a trend of first increasing and then decreasing, and the fracture toughness gradually increases. The Vickers hardness is maintained above 35.5 GPa with a ZrO₂ content of 5–15 wt%, but decreases to 32.3 GPa with a ZrO₂ content of 20 wt%. Fracture toughness gradually increases from 2.3 MPa·m^{1/2} (BZ0) to 3.96 MPa·m^{1/2} (BZ20). This is because an increase in the relative density of B₄C ceramics leads to an increase in Vickers hardness, but the presence of pores can also have a negative effect on Vickers hardness. The ZrB₂ generated in situ from nano-ZrO₂ has a pinning effect, which inhibits the growth of B₄C particles. At the same time, the residual stresses present during cooling can block the crack expansion of B₄C ceramics due to the difference in thermal expansion coefficients of B₄C and ZrB₂. Both processes are beneficial for the improvement of the fracture toughness of B₄C ceramics. As can be seen in Figure 7b, the bending strength of the B₄C ceramics shows a trend of increasing and then decreasing with an increase in ZrO₂ content. The bending strength reaches a maximum value of 404 MPa at 15 wt% ZrO₂, which is 60.3% higher than the BZ0 sample (252 MPa). The addition of nano-ZrO₂ promotes the sintering between B₄C particles and inhibits their further growth. Furthermore, the bending strength of ZrB₂ is greater than that of B₄C, ultimately improving the bending strength of the B₄C ceramics. However, when the content of ZrO₂ reaches 20 wt%, the generation of CO gas leads to an increase in the number of pores and a decrease in the density, which results in a lower bending strength. When the content of ZrO₂ is 15 wt%, the Vickers hardness, fracture toughness and bending strength of sample BZ15 are 35.5 GPa, 3.6 MPa·m^{1/2} and 404 MPa, respectively, with optimal overall performance.

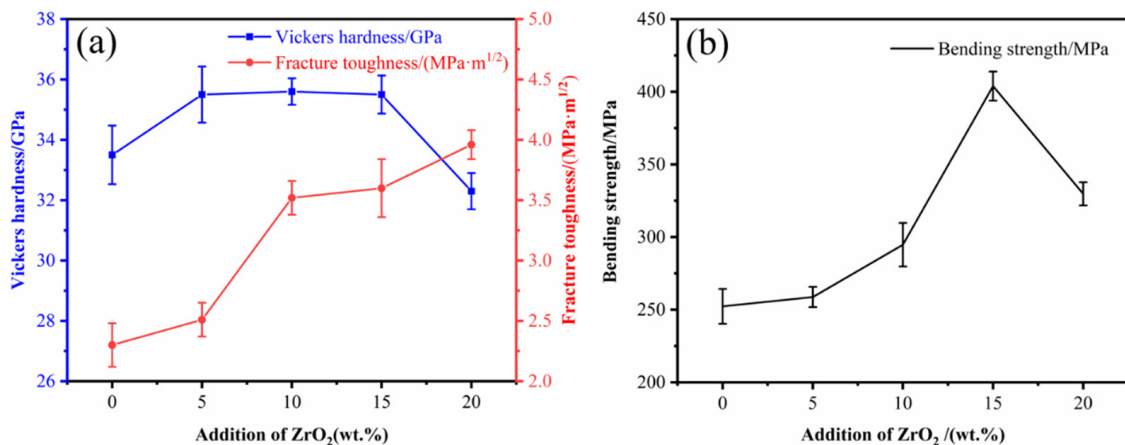


Figure 7. Mechanical properties of B₄C ceramics with different nano-ZrO₂ contents. (a) Vickers hardness and fracture toughness; (b) bending strength.

3.5. Densification and Toughening Mechanism Analysis

Crack propagation within the BZ15 sample following the Vickers hardness indentation tests is shown in Figure 8. There are obvious branching and deflection phenomena in crack extension, which can increase the energy required for crack extension and thus improve the fracture toughness of B₄C ceramics. In addition, the fracture mode of the B₄C ceramics changes from a traditional transgranular fracture to a hybrid mode of intergranular and transgranular fracture, which is beneficial for the improvement of fracture toughness.

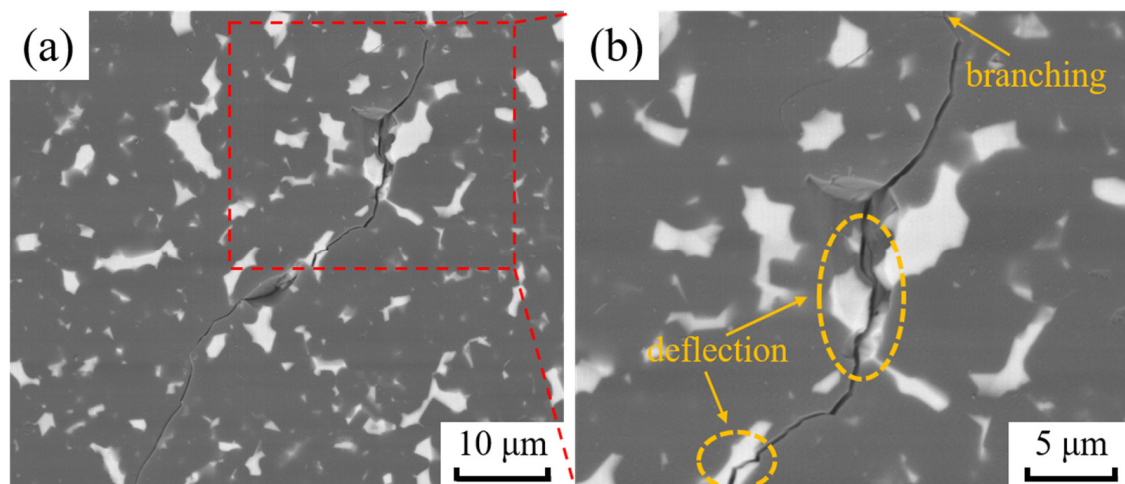


Figure 8. BSE diagrams of the crack expansion path of sample BZ15. (a) Partial view; (b) Partial enlarged view.

The different coefficients of thermal expansion between the matrix and the second phase in ceramics could induce residual stress during the cooling process. The effect of this is more obvious when the strength and elastic modulus of the second phase are higher than those of the matrix. Since the thermal expansion coefficients of B₄C and ZrB₂ are quite different, the interface between ZrB₂ and B₄C will therefore be subject to residual stress (p_i) during the cooling process [22].

$$p_i = \frac{\Delta\alpha\Delta T}{\frac{1+\nu_m}{2E_m} + \frac{1-2\nu_p}{E_p}} \quad (2)$$

where $\Delta\alpha$ is the difference between the coefficients of thermal expansion of B_4C and ZrB_2 , ΔT is the temperature difference between the cooling stages of SPS, ν is Poisson's ratio, E is elastic modulus, and the subscripts p and m stand for ZrB_2 and B_4C , respectively.

In this condition, σ_r (radial stress) and σ_t (tangential stress) are generated in the matrix at a distance r from the particles [22].

$$\sigma_r = -pi\left(\frac{R}{r}\right)^3 \quad (3)$$

and

$$\sigma_t = \frac{1}{2}pi\left(\frac{R}{r}\right)^3 \quad (4)$$

where R is the radius of the particle and r is the distance from a point in the stress field to the center of the particle. It can be seen that both σ_r and σ_t are proportional to $(R/r)^3$.

When a crack passes through this stress field, a deflection will occur, as shown in Figure 9. When second phase particles are encountered ahead of the crack, the radial tensile stress σ_r increases in the matrix (σ_r is maximal at the interface), causing the crack to deflect in the direction of the particles and reach the particle/matrix interface before propagating along the original extension direction. The combined effect of σ_r and σ_t lengthens the crack expansion path in the matrix and consumes the energy for crack expansion. Therefore, the crack deflection caused by the residual stress field produces an absolute toughening effect. Figure 8 shows that the crack extension undergoes deflection and bypass, and that there is a secondary crack generation on the primary crack, which increases the path of crack extension and consumes the energy of crack extension. If the crack propagation path is more tortuous, and the volume fraction of the second phase component which leads to crack deflection is higher, then the effect of crack deflection and toughening will be significant.

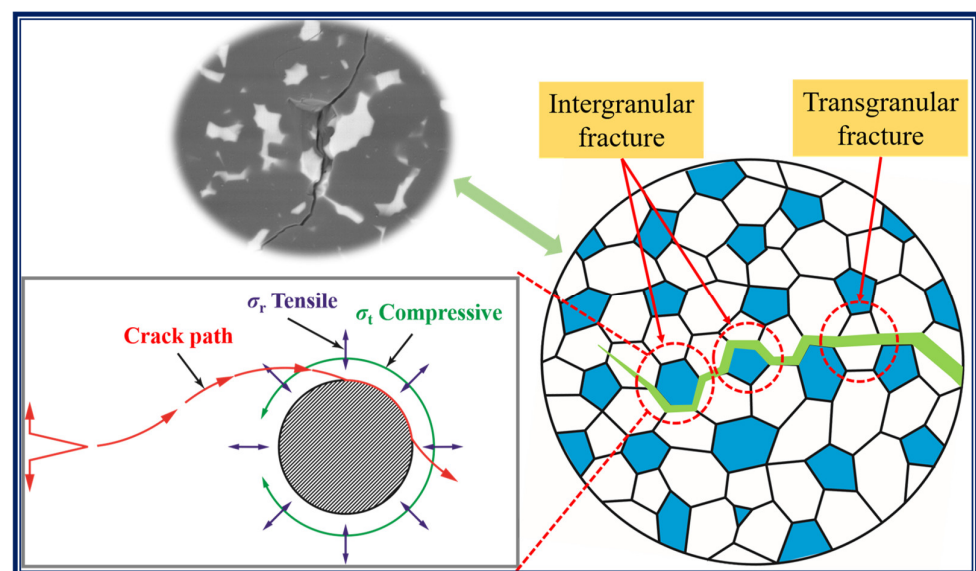


Figure 9. Schematic diagram of residual stress and crack extension in B_4C ceramics.

3.6. Comparison of Properties of B_4C Ceramics in Recent Years

The Vickers hardness and fracture toughness of B_4C ceramics prepared under different sintering methods in recent years are shown in Figure 10 [20,21,23–33]. The different sintering methods described are pressureless sintering, hot-pressure sintering and spark plasma sintering. Although the Vickers hardness and fracture toughness of B_4C ceramics are high, the sintering temperature of dense B_4C ceramics is almost above 1800 °C. In this study, B_4C ceramics are successfully prepared at 1700 °C by in situ reaction using nano-ZrO₂

as a sintering aid. The maximum values of Vickers hardness and fracture toughness are 35.5 GPa and $3.6 \text{ MPa}\cdot\text{m}^{1/2}$, respectively. The in situ-generated ZrB_2 inhibits the growth of B_4C grains, deflecting and bifurcating the cracks, thus enhancing the mechanical properties of B_4C ceramics.

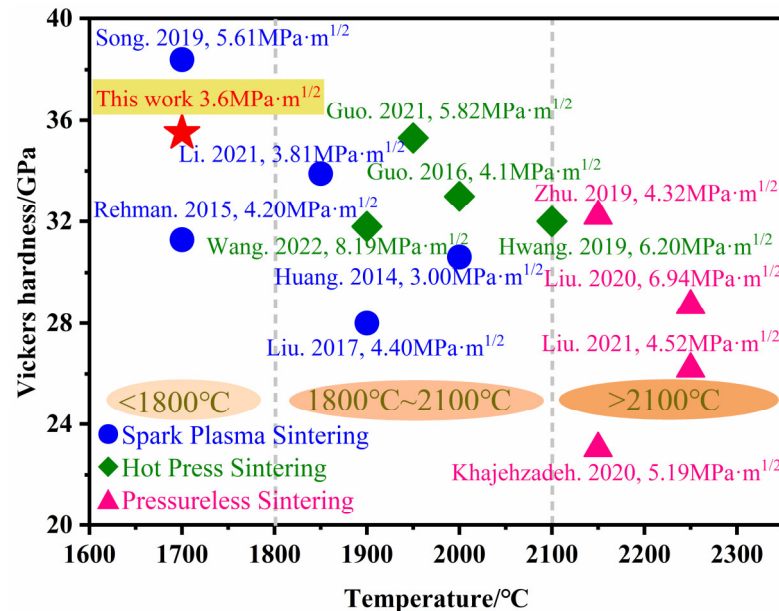


Figure 10. Comparison of the performance of B_4C ceramics in recent years [20,21,23–33].

The phase-field model of Roy shows that interfacial stress is an important factor affecting the interfacial stress distribution at interfaces and the phase-field solution [34]. Therefore, the effect of interfacial stress between B_4C and ZrB_2 , as well as the ZrO_2 phase transition process on the evolution of the nano-microstructure, must be studied in further detail. In addition, Mahdi investigated the effect of high pressure on the phase transformation [35], which may offer some insight into the effect of residual stress on ZrB_2 grain growth due to the difference in the coefficients of thermal expansion between B_4C and ZrB_2 .

4. Conclusions

In this study, B_4C ceramics were prepared by the in situ generation of ZrB_2 using SPS at low temperature. The effects of ZrB_2 on the microstructure and mechanical properties of the B_4C ceramics were characterized and tested. The following conclusions were drawn.

(1) The ceramics were composed of B_4C and ZrB_2 . The nano- ZrO_2 reacted to form fine-crystalline ZrB_2 , which was uniformly distributed in the B_4C ceramics. The in situ generation of ZrB_2 contributed to the flowability between B_4C particles, improving the sintering activity and achieving the densification of the B_4C ceramics at low temperature.

(2) The relative density, Vickers hardness and bending strength of the B_4C ceramics first increased and then decreased with the increase of ZrB_2 content, and the bulk density and fracture toughness increased continuously. The relative density was above 98.3% and the bulk density was $2.52\text{--}2.83 \text{ g/cm}^3$. When the content of ZrO_2 was 15 wt%, the Vickers hardness, fracture toughness and bending strength were $35.5 \pm 0.63 \text{ GPa}$, $3.6 \pm 0.24 \text{ MPa}\cdot\text{m}^{1/2}$ and $403 \pm 10 \text{ MPa}$, respectively, with the best overall performance.

(3) The pinning effect of ZrB_2 particles changed the fracture mode of the B_4C ceramics from traditional transgranular fracture to a hybrid mode of intergranular and transgranular fracture, which improved the bending strength of the ceramics. The high bonding strength between powders and the residual stress between B_4C and ZrB_2 led to crack deflection and crack branching during the crack propagation, which resulted in the high mechanical properties of the B_4C ceramics.

Author Contributions: Formal analysis, W.Y., J.Y., X.L., P.C., Y.Z. and B.Z.; investigation, W.Y. All authors have read and agreed to the published version of the manuscript.

Funding: This work was supported by the National Natural Science Foundation of China (Grant Nos. 51972242 and 51774218), the Science Fund for Creative Research Groups of the National Natural Science Foundation of Hubei Province (Grant No.2020CFA038) and the Key Research and Development Project of Hubei Province (Grant No. 2020BAA028) and the Young Top-notch Talent Cultivation Program of Hubei Province.

Institutional Review Board Statement: Not applicable.

Informed Consent Statement: Not applicable.

Data Availability Statement: All data generated or analyzed during this study can be made available by the corresponding author upon request.

Conflicts of Interest: The authors declare no conflict of interest.

References

1. Sha, W.; Liu, Y.; Zhou, Y.; Huang, Y.; Huang, Z. Effect of Carbon Content on Mechanical Properties of Boron Carbide Ceramics Composites Prepared by Reaction Sintering. *Materials* **2022**, *15*, 6028. [[CrossRef](#)] [[PubMed](#)]
2. Reddy, K.M.; Guo, D.; Song, S.; Cheng, C.; Han, J.; Wang, X.; An, Q.; Chen, M. Dislocation-mediated shear amorphization in boron carbide. *Sci. Adv.* **2021**, *7*, eabc6714. [[CrossRef](#)] [[PubMed](#)]
3. Thévenot, F. Boron carbide—A comprehensive review. *J. Eur. Ceram. Soc.* **1990**, *6*, 205–225. [[CrossRef](#)]
4. Chang, Y.; Sun, X.; Ma, M.; Mu, C.; Li, P.; Li, L.; Li, M.; Nie, A.; Xiang, J.; Zhao, Z. Application of hard ceramic materials B₄C in energy storage: Design B₄C@C core-shell nanoparticles as electrodes for flexible all-solid-state micro-supercapacitors with ultrahigh cyclability. *Nano Energy* **2020**, *75*, 104947. [[CrossRef](#)]
5. Qu, Z.; Yu, C.; Wei, Y.; Su, X.; Du, A. Thermal conductivity of boron carbide under fast neutron irradiation. *J. Adv. Ceram.* **2022**, *11*, 482–494. [[CrossRef](#)]
6. Domnich, V.; Reynaud, S.; Haber, R.A.; Chhowalla, M. Boron carbide: Structure, properties, and stability under stress. *J. Am. Ceram. Soc.* **2011**, *94*, 3605–3628. [[CrossRef](#)]
7. Zan, Y.; Zhou, Y.; Zhao, H.; Liu, Z.; Wang, Q.; Wang, D.; Wang, W.; Xiao, B.; Ma, Z. Enhancing high-temperature strength of (B₄C+Al₂O₃)/Al designed for neutron absorbing materials by constructing lamellar structure. *Compos. Part B Eng.* **2020**, *183*, 107674. [[CrossRef](#)]
8. Paidar, M.; Bokov, D.; Mehrez, S.; Ojo, O.O.; Ramalingam, V.V.; Memon, S. Improvement of mechanical and wear behavior by the development of a new tool for the friction stir processing of Mg/B₄C composite. *Surf. Coat. Technol.* **2021**, *426*, 127797. [[CrossRef](#)]
9. Demirskyi, D.; Vasylykiv, O. Analysis of the high-temperature flexural strength behavior of B₄C–TaB₂ eutectic composites produced by in situ spark plasma sintering. *Mater. Sci. Eng. A* **2017**, *697*, 71–78. [[CrossRef](#)]
10. Zhang, W. A review of tribological properties for boron carbide ceramics. *Prog. Mater. Sci.* **2021**, *116*, 100718. [[CrossRef](#)]
11. Zhao, X.; Zou, J.; Ji, W.; Wang, A.; He, Q.; Xiong, Z.; Wang, W.; Fu, Z. Processing and mechanical properties of B₄C–SiCw ceramics densified by spark plasma sintering. *J. Eur. Ceram. Soc.* **2022**, *42*, 2004–2014. [[CrossRef](#)]
12. Jin, X.; Tang, C.; Li, Q.; Wang, D.; Ding, X.; Ran, S. Densification and strengthening mechanism in spark plasma sintering of B₄C–VB₂ ceramics via carbide boronizing. *Ceram. Int.* **2022**, *48*, 26452–26459. [[CrossRef](#)]
13. Ren, D.; Deng, Q.; Wang, J.; Yang, J.; Li, Y.; Shao, J.; Li, M.; Zhou, J.; Ran, S.; Du, S. Synthesis and properties of conductive B₄C ceramic composites with TiB₂ grain network. *J. Am. Ceram. Soc.* **2018**, *101*, 3780–3786. [[CrossRef](#)]
14. Tu, R.; Li, N.; Li, Q.; Zhang, S.; Zhang, L.; Goto, T. Effect of microstructure on mechanical, electrical and thermal properties of B₄C–HfB₂ composites prepared by arc melting. *J. Eur. Ceram. Soc.* **2016**, *36*, 3929–3937. [[CrossRef](#)]
15. Yu, H.; Namini, A.S.; Shakeri, M.S.; Delbari, S.A.; Van Le, Q.; Cha, J.H.; Kim, S.Y.; Jang, H.W.; Lee, S.-H.; Swiatkowska-Warkocka, Z. HRTEM study and mechanical properties of ZrB₂–SiC composite: An insight into in-situ carbon formation over the SPS process. *Int. J. Refract. Met. Hard Mater.* **2022**, *104*, 105789. [[CrossRef](#)]
16. Cheng, X.; He, R.; Qu, Z.; Ai, S.; Fang, D. High temperature flexural strength of B₄C–ZrB₂ ceramic at 1000–1600 °C in air. *Ceram. Int.* **2015**, *41*, 14574–14578. [[CrossRef](#)]
17. Yang, Q.; Hwang, C.; Khan, A.U.; Domnich, V.; Gronske, E.D.; Haber, R.A. Anisotropy and residual stress in B₄C–ZrB₂ eutectic. *Mater. Charact.* **2019**, *155*, 109797. [[CrossRef](#)]
18. He, R.; Jing, L.; Qu, Z.; Zhou, Z.; Ai, S.; Kai, W. Effects of ZrB₂ contents on the mechanical properties and thermal shock resistance of B₄C–ZrB₂ ceramics. *Mater. Des.* **2015**, *71*, 56–61. [[CrossRef](#)]
19. Lin, X.; Ai, S.; Feng, Y.; Gao, D.; Guo, X.; Liu, Y.; Xie, B.; Gong, H.; Zhang, Y. Fabrication and properties of in-situ pressureless-sintered ZrB₂/B₄C composites. *Ceram. Int.* **2017**, *43*, 15593–15596. [[CrossRef](#)]
20. Guo, W.; Wu, L.; You, Y.; Lin, H.; Zhang, G. Three-step reactive hot pressing of B₄C–ZrB₂ ceramics. *J. Eur. Ceram. Soc.* **2016**, *36*, 951–957. [[CrossRef](#)]

21. Rehman, S.S.; Ji, W.; Fu, Z.; Wang, W.; Wang, H.; Asif, M.; Zhang, J. In situ synthesis and sintering of B_4C/ZrB_2 composites from B_4C and ZrH_2 mixtures by spark plasma sintering. *J. Eur. Ceram. Soc.* **2015**, *35*, 1139–1145. [[CrossRef](#)]
22. Wachtman, J.B.; Cannon, W.R.; Matthewson, M.J. *Mechanical Properties of Ceramics*; John Wiley & Sons: Hoboken, NJ, USA, 2009.
23. Li, P.; Ma, M.; Wu, Y.; Zhang, X.; Chang, Y.; Zhuge, Z.; Sun, L.; Hu, W.; Yu, D.; Xu, B. Preparation of dense B_4C ceramics by spark plasma sintering of high-purity nanoparticles. *J. Eur. Ceram. Soc.* **2021**, *41*, 3929–3936. [[CrossRef](#)]
24. Song, Q.; Zhang, Z.-H.; Hu, Z.-Y.; Yin, S.-P.; Wang, H.; Ma, Z.-W. Microstructure and mechanical properties of super-hard B_4C ceramic fabricated by spark plasma sintering with $(Ti_3SiC_2 + Si)$ as sintering aid. *Ceram. Int.* **2019**, *45*, 8790–8797. [[CrossRef](#)]
25. Liu, G.; Chen, S.; Zhao, Y.; Fu, Y.; Wang, Y. The effect of transition metal carbides MeC (Me = Ti, Zr, Nb, Ta, and W) on mechanical properties of B_4C ceramics fabricated via pressureless sintering. *Ceram. Int.* **2020**, *46*, 27283–27291. [[CrossRef](#)]
26. Wang, A.; Hu, L.; Guo, W.; Zhao, X.; Shi, Y.; He, Q.; Wang, W.; Wang, H.; Fu, Z. Synergistic effects of TiB_2 and graphene nanoplatelets on the mechanical and electrical properties of B_4C ceramic. *J. Eur. Ceram. Soc.* **2022**, *42*, 869–876. [[CrossRef](#)]
27. Liu, G.; Chen, S.; Zhao, Y.; Fu, Y.; Wang, Y. Effect of Ti and its compounds on the mechanical properties and microstructure of B_4C ceramics fabricated via pressureless sintering. *Ceram. Int.* **2021**, *47*, 13756–13761. [[CrossRef](#)]
28. Hwang, C.; DiPietro, S.; Xie, K.Y.; Yang, Q.; Celik, A.M.; Khan, A.U.; Domnich, V.; Walck, S.; Hemker, K.J.; Haber, R.A. Small amount TiB_2 addition into B_4C through sputter deposition and hot pressing. *J. Am. Ceram. Soc.* **2019**, *102*, 4421–4426. [[CrossRef](#)]
29. Guo, W.; Wang, A.; He, Q.; Tian, T.; Liu, C.; Hu, L.; Shi, Y.; Liu, L.; Wang, W.; Fu, Z. Microstructure and mechanical properties of B_4C-TiB_2 ceramic composites prepared via a two-step method. *J. Eur. Ceram. Soc.* **2021**, *41*, 6952–6961. [[CrossRef](#)]
30. Khajehzadeh, M.; Ehsani, N.; Baharvandi, H.R.; Abdollahi, A.; Bahaaddini, M.; Tamadon, A. Thermodynamical evaluation, microstructural characterization and mechanical properties of B_4C-TiB_2 nanocomposite produced by in-situ reaction of nano- TiO_2 . *Ceram. Int.* **2020**, *46*, 26970–26984. [[CrossRef](#)]
31. Liu, Z.; Wang, D.; Li, J.; Huang, Q.; Ran, S. Densification of high-strength B_4C-TiB_2 composites fabricated by pulsed electric current sintering of $TiC-B$ mixture. *Scr. Mater.* **2017**, *135*, 15–18. [[CrossRef](#)]
32. Huang, S.; Vanmeensel, K.; Vleugels, J. Powder synthesis and densification of ultrafine B_4C-ZrB_2 composite by pulsed electrical current sintering. *J. Eur. Ceram. Soc.* **2014**, *34*, 1923–1933. [[CrossRef](#)]
33. Zhu, Y.; Wang, F.; Wang, Y.; Cheng, H.; Luo, D.; Zhao, Y. Mechanical properties and microstructure evolution of pressureless-sintered B_4C-SiC ceramic composite with CeO_2 additive. *Ceram. Int.* **2019**, *45*, 15108–15115. [[CrossRef](#)]
34. Roy, A.M. Influence of interfacial stress on microstructural evolution in NiAl alloys. *JETP Lett.* **2020**, *112*, 173–179. [[CrossRef](#)]
35. Javanbakht, M. High pressure phase evolution under hydrostatic pressure in a single imperfect crystal due to nanovoids. *Materialia* **2021**, *20*, 101199. [[CrossRef](#)]